Solid-State Electronics 52 (2008) 1563–1568

Contents lists available at ScienceDirect

Solid-State Electronics

journal homepage: www.elsevier.com/locate/sse

Two-band $\mathbf{k} \cdot \mathbf{p}$ model for the conduction band in silicon: Impact of strain and confinement on band structure and mobility

V. Sverdlov *, G. Karlowatz, S. Dhar, H. Kosina, S. Selberherr

Institute for Microelectronics, TU Wien, Gußhausstr. 27–29, 1040 Vienna, Austria

ARTICLE INFO

Article history:
Received 9 May 2008
Accepted 7 June 2008
Available online 27 July 2008

Review of this manuscript was arranged by A. Iliadis, C. Richter, and A. Zaslavsky

Keywords:
$\mathbf{k} \cdot \mathbf{p}$ model
Ultra-thin body FETs
Subband quantization
Non-parabolicity
Mobility
Monte carlo simulations

ABSTRACT

The lowest conduction band of Si is often approximated by three pairs of equivalent parabolic valleys located near the *X*-points of the Brillouin zone. There are recent experimental indications that the effective mass depends on shear strain and the silicon film thickness. The parabolic band structure ignores these effects completely. By comparison with numerical pseudopotential calculations, we show that the recently evaluated two-band $\mathbf{k} \cdot \mathbf{p}$ model accurately describes the dependences of the valley shifts and the effective masses on the shear strain component. Furthermore, we demonstrate that the two-band model is valid in a larger portion of the Brillouin zone as compared to the parabolic approximation with strain dependent effective masses and can be successfully used to describe analytically the subband dispersions in ultra-thin Si films, with or without strain. In the latter case, the model provides an analytical expression for the thickness-dependent non-parabolicity parameter in the unprimed subbands. Finally, the low-field mobility with the dependence of the non-parabolicity parameter on the film thickness taken into account is compared with the mobility computed with the bulk value of the non-parabolicity parameter.

© 2008 Elsevier Ltd. All rights reserved.

1. Introduction

Continuing downscaling of transistor feature size is the key for the tremendous success of CMOS technology [1]. The scalability allows to put more transistors per unit area, while increasing transistor performance and reducing costs per operation. An anticipated performance enhancement was achieved at the expenses of the increase in subthreshold and gate leakage currents. Keeping power dissipation due to leakage currents under control forced device engineers to look for new technological solutions in order to deliver projected performance gain. At the 90 nm technology node, stress technique was introduced to enhance performance while keeping the MOSFET design intact. Since then, stress-induced mobility engineering has become a key technique to increase the performance of modern CMOS devices.

In biaxially stressed devices the electron mobility can be nearly doubled [2]. The reason for the mobility enhancement is the stress-induced band structure modification. The conduction band in Si is commonly approximated by three pairs of equivalent valleys with their minima located close to the *X*-points of the Brillouin zone. Close to the minima the electron dispersion is well described by the effective mass approximation. The degeneracy between the six equivalent valleys is lifted due to stress-induced valley shifts. This reduces inter-valley scattering. In case of tensile biaxial stress applied in the (100) plane the four in-plane valleys move up in energy and become depopulated. The two out-of-plane valleys become more populated. Since electrons in the out-of-plane valleys have favorable conductivity mass and because of reduced inter-valley scattering between out-of-plane and in-plane valleys, the electron mobility is increased [3].

Biaxial stress is usually introduced globally by growing Si epitaxially on a relaxed SiGe substrate. This method, however, cannot provide comparable on-currents in n- and p-MOSFETs required by CMOS technology and is not used in mass production. Instead, the semiconductor industry employs stress techniques compatible with existing CMOS fabrication process. Stress in the channel of a MOSFET is created by using local stressors in the source and drain and additional cap layers. Although already successfully used in mass production, the technologically relevant [110] stress has received little attention within the research community. Only recently the electron mobility modification under stress was systematically investigated experimentally [4].

A shear distortion of the Si crystal lattice inherent to [110] uniaxial stress induces, apart from the nonlinear valley shift [5–7], a more pronounced modification in the conduction band. Shear strain changes substantially both the longitudinal [6,7] and transversal [4,6–8] effective masses in the out-of-plane valley minima. The decrease of the mass in the transport direction along tensile [110] stress and the valley repopulation due to the valley shifts

* Corresponding author.
E-mail address: sverdlov@iue.tuwien.ac.at (V. Sverdlov).

0038-1101/$ - see front matter © 2008 Elsevier Ltd. All rights reserved.
doi:10.1016/j.sse.2008.06.019

lead to the mobility enhancement [4,6,7]. The mobility increase is slightly hampered by an increase of the non-parabolicity parameter with shear strain [7].

Double-gate silicon-on-insulator (SOI) transistors with ultra-thin Si body (UTB) are good candidates for the far-end ITRS roadmap scaling [9]. Superior electrostatic channel control helps reducing the leakage current and allows scaling the channel length down to 2.5 nm [10], while maintaining reasonable subthreshold slope, satisfactory DIBL, and acceptable gain. Due to size quantization in thin Si films the energy spectrum of each valley is split into a set of two-dimensional subbands. In [0 0 1] Si films two sets of subband ladders are formed. The unprimed ladder originates from the two out-of-plane valleys and is therefore two-fold degenerate. The primed ladder is obtained from the four in-plane valleys and is four-times degenerate. Due to the large quantization mass m_l the subband energies in the unprimed ladder are lower than that in the primed ladder, where the quantization mass is smaller, $m_t < m_l$. Because of the large separation between primed and unprimed subbands only the unprimed ladder is occupied in UTB FETs. The smaller transversal mass m_t is the conductivity mass of unprimed subbands, which favors their superior mobility over the primed ones. If we now apply tensile uniaxial stress in the [1 1 0] transport direction, the electron mobility enhancement is due to the shear strain induced decrease of the conductivity mass [4,6,7]. The role of shear strain in determining the subband energies has not yet been analyzed.

We demonstrate that the two-band $\mathbf{k}\cdot\mathbf{p}$ model [7,8,11] not only describes accurately the dependences of the valley shifts and the effective masses on the shear strain component. By comparing the model to results from the empirical pseudopotential method (EPM) we show that the two-band $\mathbf{k}\cdot\mathbf{p}$ model predicts the correct energy dispersion in a wider range of momenta in the Brillouin zone capturing non-parabolicity effects due to the interaction between the two lowest conduction bands. Because the model provides an analytical expression for the energy dispersion also in the presence of shear strain, it allows to explore analytically the quantized subband dispersion in UTB FETs. An example of the dependence of subband energy on shear strain is presented. The model also predicts the dependence of the subband non-parabolicity parameter on UTB film thickness t. This dependence leads to a pronounced suppression of the low field mobility in UTB FETs, which helps to bring the simulated UTB FET mobility, with scattering parameters calibrated to reproduce the inversion layer mobility, closer to the measured quantities and, therefore, must be taken into account.

In the next section, we briefly outline the analytical two-band $\mathbf{k}\cdot\mathbf{p}$ model and verify it against the EPM numerical calculations. Then we discuss the influence of shear strain on subband structure. Finally, we investigate the dependence of the non-parabolicity parameter on film thickness and how it may affect the low-field mobility.

2. Comparison of the two-band k · p model with EPM results

The dispersion relations of the first two conduction bands in the vicinity of the [0 0 1] X-point can be obtained for arbitrary stress within the two-band $\mathbf{k}\cdot\mathbf{p}$ model [7,8,11]:

$$E_{1,2}(\mathbf{k}) = \frac{\hbar^2 k_z^2}{2m_l} + \frac{\hbar^2(k_x^2+k_y^2)}{2m_t} + \delta E_C \pm \sqrt{\left(\frac{\Delta k_z}{2k_0}\right)^2 + \left(D\varepsilon_{xy} - \frac{\hbar^2 k_x k_y}{M}\right)^2}. \tag{1}$$

The minus sign denotes the lowest (Δ_1) and plus the second (Δ_2') conduction band. In this expression the values of energy $E(\mathbf{k})$ and k_z are measured from the X-point, m_t stands for the transversal and m_l for the longitudinal effective masses, $k_0 = 0.15 \times 2\pi/a$, where a is the Si lattice constant, is the position of the energy minimum of (1) relative the X-point in unstrained Si, $\Delta = 2\hbar^2 k_0^2/m_l = 0.53$ eV is the energy gap between the conduction bands Δ_1 and Δ_2' at k_0, and the parameter M is determined by the interband matrix elements:

$$\frac{1}{M} = \frac{1}{m_0^2}\left|\sum_{l\neq\Delta_1,\Delta_2'} \frac{(p_x)_{\Delta_1 l}(p_y)_{l\Delta_2'}}{E_l(k_0)-E_{\Delta_1}(k_0)} + \frac{(p_x)_{\Delta_1 l}(p_y)_{l\Delta_2'}}{E_l(k_0)-E_{\Delta_2'}(k_0)}\right|.$$

The value of M is computed using the pseudopotential method at the valley minimum $k_z = k_0$. Obtained value $M = 0.235m_0$ is close (but not equal) to $M = m_t/(1 - m_t/m_0)$ reported in [8].

The dispersion relation (1) describes the dependence of $E(\mathbf{k})$ on the strain tensor $\varepsilon_{\alpha\beta}$, where $\alpha, \beta = x, y, z$. The shift δE_C of the [0 0 1] valley depends linearly on diagonal strain components:

$$\delta E_C = \Xi_d(\varepsilon_{xx} + \varepsilon_{yy} + \varepsilon_{zz}) + \Xi_u \varepsilon_{zz},$$

where Ξ_d is the dilation and Ξ_u the uniaxial deformation potential for the conduction band minimum.

The shear strain component ε_{xy}, which is created by [1 1 0] uniaxial stress, lifts the degeneracy of the conduction bands Δ_1 and Δ_2' at the X-point ($k_z = 0$). The gap

$$|E_2(0) - E_1(0)| = 2D|\varepsilon_{xy}|$$

opens, where the shear deformation potential $D = 14$ eV is introduced. From (1) it follows that the minimum $k_{\min}$ along the k_z axis of the [0 0 1] valley depends on shear strain. First, it moves closer to the X point:

$$k_{\min} = k_0\sqrt{1-\eta^2}, \quad |\eta| < 1, \tag{2}$$

where a dimensionless shear strain η is introduced as

$$\eta = \frac{2D\varepsilon_{xy}}{\Delta}.$$

For $|\eta| \geqslant 1$ the valley minimum rests at the X-point: $k_{\min} = 0$. The minimum of the [0 0 1] valley also moves down in energy with respect to the remaining four fold degenerate valleys. For $|\eta| \leqslant 1$ the η dependence of the valley shift is quadratic [7,6,5], while it becomes linear for $|\eta| \geqslant 1$:

$$\Delta E_{\text{shear}} = \begin{cases} -\frac{\Delta}{4}\eta^2, & |\eta| < 1 \\ -\frac{\Delta}{4}(2|\eta| - 1), & |\eta| > 1 \end{cases} \tag{3}$$

The analytical conduction band model (1) allows to obtain the dependences of the effective masses on shear strain ε_{xy} in the [0 0 1] valleys [4,6–8,11]. The transversal mass develops strong anisotropy for nonzero ε_{xy}. At the band minimum the mass m_{t1} across and m_{t2} along the [1 1 0] stress direction are:

$$\frac{m_{t1}(\eta)}{m_t} = \begin{cases} \left(1 - \eta\frac{m_t}{M}\right)^{-1}, & |\eta| < 1 \\ \left(1 - \operatorname{sgn}(\eta)\frac{m_t}{M}\right)^{-1}, & |\eta| > 1 \end{cases} \tag{4}$$

$$\frac{m_{t2}(\eta)}{m_t} = \begin{cases} \left(1 + \eta\frac{m_t}{M}\right)^{-1}, & |\eta| < 1 \\ \left(1 + \operatorname{sgn}(\eta)\frac{m_t}{M}\right)^{-1}, & |\eta| > 1 \end{cases} \tag{5}$$

Here, sgn is the sign function. The dependence of the longitudinal mass on shear strain can also be obtained:

$$\frac{m_l(\eta)}{m_l} = \begin{cases} (1 - \eta^2)^{-1}, & |\eta| < 1, \\ \left(1 - \frac{1}{|\eta|}\right)^{-1}, & |\eta| > 1. \end{cases} \tag{6}$$

The analytical expression (1) predicts dispersions not only close to the band minimum. Comparison of the analytical k_z dispersion (1) to the results of the numerical empirical pseudopotential calcula-

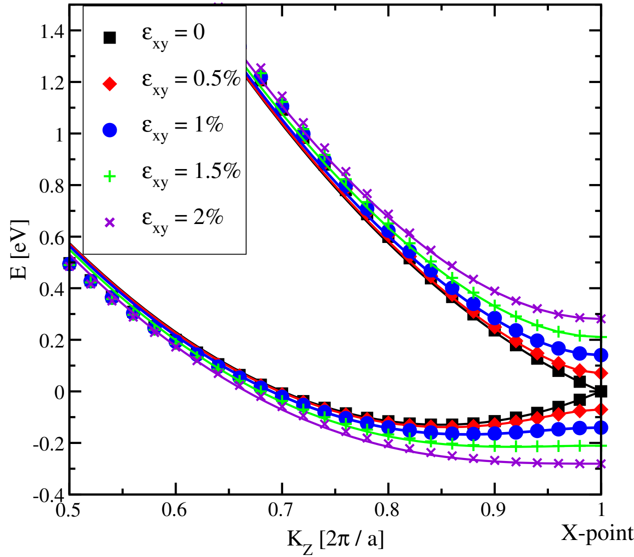

Fig. 1. Comparison of the k_z dispersions obtained from the analytical model (1) (lines) and the EPM calculations (symbols), for several values of shear strain. In the analytical dispersion (1) k_z is counted from the X-point ($k_z = 2\pi/a - K_z$), D= 14 eV and $m_l = 0.9m_0$.

tions for the [0 0 1] valley are displayed in Fig. 1 for several values of shear strain. For EPM calculations the pseudopotential parameters from [12] are used. In order to fit the analytical dispersion to the EPM data, the value $m_l = 0.9m_0$, where m_0 is the electron mass, was chosen for all strain values. It is seen that the analytical dispersion (1) (lines) reproduces the EPM data (symbols) excellently in a large interval $|k_z - k_0| < 0.25(2\pi/a)$ around the minimum value k_0 even at large strain $\varepsilon_{xy} = 2\%$, when the valley minimum is at the X-point. Therefore, we conclude that (1) describes the k_z dispersion up to the energy of approximately 0.5 eV from the valley minimum. We also notice that the dispersion relation (1) describes accurately the band degeneracy lifting at the X-point, where the form (1) is dictated by symmetry [11] and is therefore exact.

In order to validate the use of (1) in a larger portion of the Brillouin zone, we now compare the dispersions in xy plane. Results of (1) and numerical EPM calculations are shown in Fig. 2. Panel (a) displays a good agreement between the analytical and numerical dispersions up to 0.5 eV from the valley minimum in unstressed Si. Panel (b) demonstrates a good agreement of analytical band structure to the numerical one in the case when the tensile stress of 150 MPa in [1 1 0] is combined with compressive stress in [$\bar{1}$ 1 0] direction. The chosen strain configuration allows to generate only the shear strain component. Comparison with the analytical band structure within the parabolic effective mass approximation with strain-dependent masses (4) and (5) is added to panel (c). Agreement between all the three methods is good for energies close to the valley minimum. At energies larger than 40 meV the parabolic approximation becomes less accurate, while the analytical two-band $\mathbf{k}\cdot\mathbf{p}$ model (1) closely follows the numerical dispersion. Because the $\mathbf{k}\cdot\mathbf{p}$ model is valid in a larger portion of the Brillouin zone, we use the model to investigate the dispersion of the quantized subbands in UTB FETs in the next section.

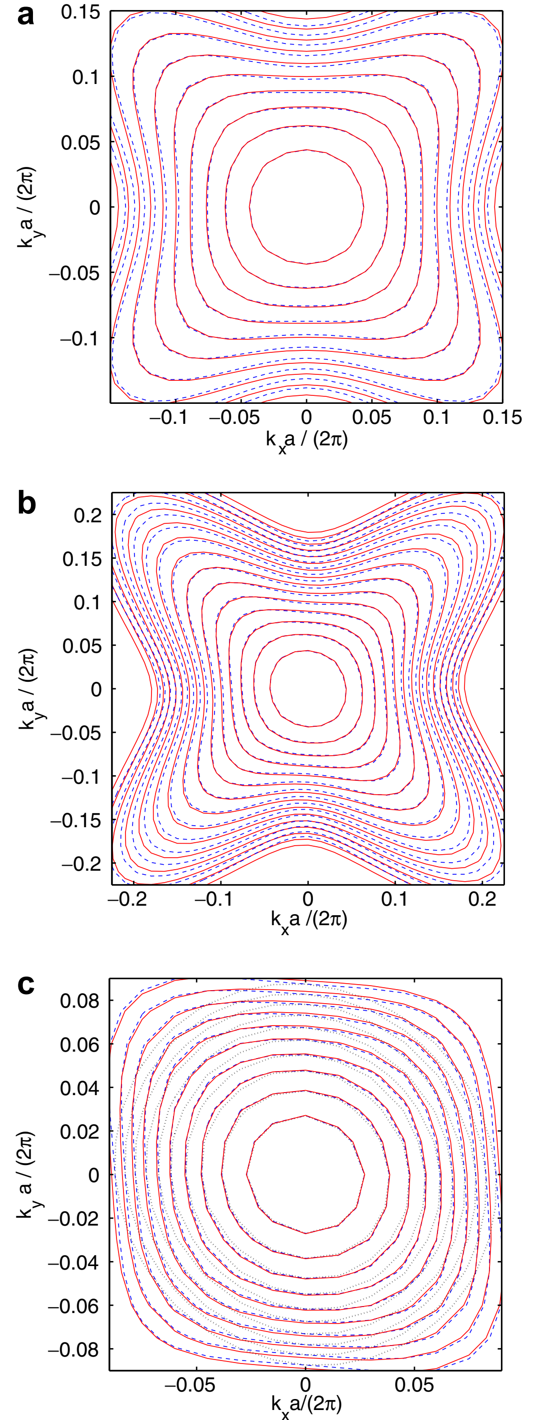

Fig. 2. Comparison between the analytical model (1) (dashed lines) and the EPM calculations (solid lines). The contour lines are spaced at 50 meV for panels (a) and (b) and 20 meV for panel (c). No stress is applied at panel (a) tensile stress in [1 1 0] and compressive stress in [$\bar{1}$ 1 0] direction of 150 MPa in each direction is applied at the panels (b) and (c), respectively. The parabolic approximation with strain dependent effective masses is also shown in panel (c) (dotted lines).

3. Subband structure in strained UTB FETs

Shear strain may affect the subband energies in UTB Si films. In order to estimate this effect, we assume that the potential inside the Si film of thickness t can be approximated by the square well potential with infinite walls at the Si/SiO_2 interfaces. The wave function in the conduction band is taken of the form:

$$\psi(x,y,z) = A\sum_{j=1,2}(-1)^{j-1}\exp(\mathrm{i}k_jz)\exp(\mathrm{i}k_xx+\mathrm{i}k_yy). \quad (7)$$

It has the usual plane wave structure in the x, y plane with fixed k_x, k_y. The values k_j of the wave function in the quantization direction must be determined from the conditions that the wave function must vanish at the interfaces:

$\psi(x, y, \pm t/2) = 0$

and that the corresponding energies are equal:

$E(k_x, k_y, k_1) = E(k_x, k_y, k_2) = E.$

The values of k_j are found from (1), when it is resolved for k_z. The corresponding equation is

$$\hbar^4 k_z^4 - 4(m_l E + \hbar^2 k_0^2)k_z^2 + 4m_l^2(E^2 - \delta^2) = 0, \tag{8}$$

where δ is defined as:

$$\delta = \hbar^2 k_x k_y / M - D\varepsilon_{xy}. \tag{9}$$

The solution for k_z is easily found when $\delta = 0$:

$$k_z^2 = \left(k_0 \pm \sqrt{\frac{2m_l E}{\hbar^2} + k_0^2}\right)^2. \tag{10}$$

By choosing the values $k_{1,2} = k_0 \pm \sqrt{2m_l E/\hbar^2 + k_0^2}$, the wave function (7) becomes zero at the interfaces if

$$\sqrt{\frac{2m_l E_n^0}{\hbar^2} + k_0^2} = \frac{\pi n}{t}, \quad n = 1, 2, 3, \ldots$$

from which the standard subband dispersions are

$$E_n^0(k_x, k_y) = E_n^0 + \frac{\hbar^2(k_x^2 + k_y^2)}{2m_l}, \tag{11}$$

where

$$E_n^0 = \frac{\hbar^2 \pi^2 n^2}{2m_l t^2} - \frac{\Delta}{4}$$

are the subband energies relative to the X-point.

By analogy, for $\delta \neq 0$ one looks for a solution of (8) in the form:

$$k_{1,2} = \xi \pm \frac{\pi n}{t}. \tag{12}$$

The subband energies are

$$E_n(k_x, k_y) = E_n^0(k_x, k_y) - \frac{\delta^2}{\Delta} \frac{1}{1 - \frac{\pi^2 n^2}{k_0^2 t^2}}, \tag{13}$$

while ξ depends on δ:

$$\xi = k_0 \sqrt{1 - \frac{4\delta^2}{\Delta^2} \frac{1}{1 - \frac{\pi^2 n^2}{k_0^2 t^2}}}. \tag{14}$$

The obtained expressions (13) and (14) are valid when (8) has got four real roots, which results in the conditions

$$\frac{\pi^2 n^2}{k_0^2 t^2} \leqslant 1 - \frac{2|\delta|}{\Delta}, \qquad \frac{\pi^2 n^2}{k_0^2 t^2} \geqslant 1 + \frac{2|\delta|}{\Delta}. \tag{15}$$

We note that the dispersion relation (13) may become less accurate close to its validity region defined in (15) due to the used ansatz (7) for the wave function. In this approximation the two valleys with the dispersion (1) are considered to be independent. Coupling between the valleys introduces the valley splitting in a confined system and prevents from finding simple analytical expressions for subband dispersions. At the same time the valley splitting does not significantly affect the subband effective masses, at least for small and moderate strain values. In order to obtain the analytical expression for the subband effective masses and the non-parabolicity parameter we neglect the valley splitting in this study.

Examples of quantization for $\delta = 0$ and $\delta = 53$ m eV for a film of the thickness $t = 4.9$ nm are shown in Fig. 3. By means of Fig. 3 the solution of (8) in the form (12)–(14) allows a simple graphic interpretation: the energy E_n and the position ξ are determined from the condition:

$$E\left(\xi + \frac{\pi n}{t}\right) = E\left(\xi - \frac{\pi n}{t}\right) = E_n.$$

Depending on the parameters, Eq. (8) may have either four or two real roots. In case of four roots, they are combined in pairs (12) around the corresponding minimum (14) in such a way that within the pair each member has the group velocity of opposite sign. In case of only two real roots, the minimum $\xi = 0$, and the subband energy is determined by (1) with $k_z = \pi\, n/t$. These solutions may exist only for finite δ when the gap at the X-point is opened.

Eq. (13) provides the non-parabolic dispersion relation of the unprimed subbands. In particular, the subband energy in strained Si film is shifted with respect to E_n^0:

$$E_n(\eta) = E_n^0 - \frac{\Delta}{4}\eta^2 \frac{1}{1 - \frac{\pi^2 n^2}{k_0^2 t^2}}. \tag{16}$$

Taking the bulk band shift (3) into account (16) can be rewritten for $(\pi n/k_0 t)^2 \ll 1$ as

$$E_n(\eta) = \frac{\pi^2 n^2}{2m_l(\eta)t^2} - \Delta E_{\text{shear}}, \tag{17}$$

where $m_l(\eta)$ is defined by (6). Shear strain also modifies the in-plane effective mass m_t, making it anisotropic. Interestingly, the modification of the effective mass also depends on UTB thickness t. As in the bulk case, the principal axis of anisotropy are [1 1 0] and [$\bar{1}$ 1 0]. The mass across m_{n1} and along m_{n2} the [1 1 0] stress direction now are

$$\frac{m_{n1}(\eta, t)}{m_t} = \left(1 - \eta \frac{m_t}{M} \frac{1}{1 - \frac{\pi^2 n^2}{k_0^2 t^2}}\right)^{-1}, \tag{18}$$

$$\frac{m_{n2}(\eta, t)}{m_t} = \left(1 + \eta \frac{m_t}{M} \frac{1}{1 - \frac{\pi^2 n^2}{k_0^2 t^2}}\right)^{-1}. \tag{19}$$

Expressions (13), (18) and (19) are subject to the conditions $|\eta| \leqslant 1$ and (15).

4. Dependence of the subband non-parabolicity parameter on UTB FET thickness

For vanishing shear strain ($\varepsilon_{xy} = 0$) expression (13) provides a non-parabolic dispersion relation for unprimed subbands as

$$E_n(k_x, k_y) = \frac{\hbar^2 \pi^2 n^2}{2m_l t^2} + \frac{\hbar^2(k_x^2 + k_y^2)}{2m_l} - \frac{\hbar^4 k_x^2 k_y^2}{M^2 \Delta} \frac{1}{1 - \frac{\pi^2 n^2}{k_0^2 t^2}} - \frac{\Delta}{4}. \tag{20}$$

Besides the usual parabolic dependence on k_x, k_y, the dispersion (20) contains a fourth order term, which modifies the energy dependence of the density of states. Such deviation is usually accounted for by the non-parabolicity parameter α_n. An isotropic non-parabolic dispersion including the non-parabolicity parameter is usually taken in the form:

$$\frac{\hbar^2(k_x^2 + k_y^2)}{2m_l} = E_n(k_x, k_y)(1 + \alpha_n E_n(k_x, k_y)). \tag{21}$$

Assuming the non-parabolic term in (20) to be small, we average it, as in [13], over the equienergy surface $E_n^0(k_x, k_y) = E$. The obtained isotropic dependence on $k_x^2 + k_y^2$ is re-expressed via $E = E_n^0(k_x, k_y)$, using again the smallness of the non-parabolic term. As a result

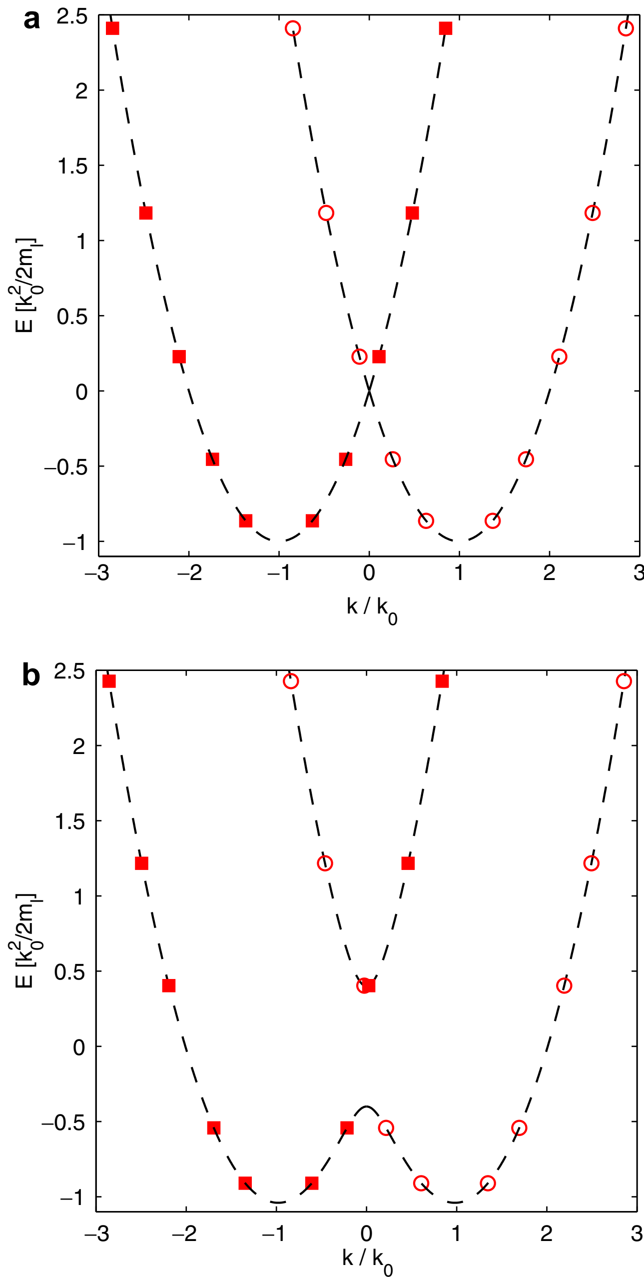

Fig. 3. Quantization energies of the unprimed ladder for a (001) Si film of t = 4.9 nm. No strain is applied at panel (a), while a shear strain $D\varepsilon_{xy}$ = 53 meV is set at the panels (b).

one obtains the following expression for the non-parabolicity parameter:

$$\alpha_n(t) = \alpha_0 \frac{1}{1 - \frac{\pi^2 n^2}{k_0^2 t^2}}, \tag{22}$$

where

$$\alpha_0 = \frac{1}{2\Delta}\left(\frac{m_t}{M}\right)^2.$$

The estimated value of α_0 = 0.63 eV^{-1} is close to the phenomenological value α_0 = 0.5 eV^{-1} [13] obtained experimentally. It is interesting to note that the non-parabolicity is determined by the strength of interaction of the lowest conduction band to the closest band, which is inversely proportional to the gap Δ. The dependence of the non-parabolicity parameter on the film thickness t is shown in Fig. 4.

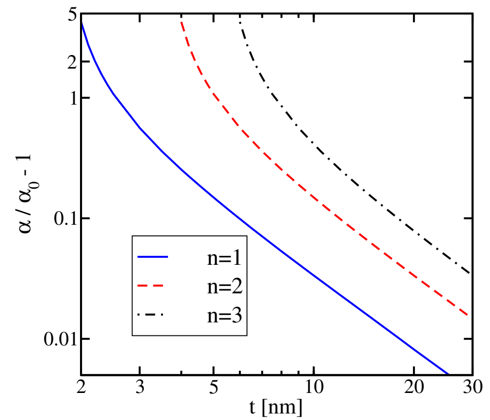

Fig. 4. Dependence of the non-parabolicity parameter on the film thickness for the three lowest unprimed subbands.

5. Low-field mobility in UTB Si films

Through the modification of the density-of states, the non-parabolicity parameter affects the scattering rates, and therefore the mobility of the system. As example we consider the mobility in a double-gate FET with a thin Si body. The subband energies and the corresponding wave functions are calculated from the Schrödinger equation using the parabolic approximation also for the [001] valleys with the effective mass m_l defined by (6) and m_t by (18) and (19), respectively. The Schrödinger equation is solved self-consistently with the Poisson equation for each value of the effective field [14]. The wave functions obtained are used to evaluate the scattering rates. Our transport calculations account for electron–phonon [13,15] and surface roughness scattering. For the surface roughness scattering matrix elements we use the original formulation by Prange and Nee [16–19]. A Gaussian correlation function [20] for the surface roughness is assumed. The zero-field Monte Carlo algorithm [21,22] which accounts for the Pauli blocking factor in the scattering rates was used to evaluate the low-field mobility.

Results of the mobility simulations in an UTB FET, with and without the dependence of the non-parabolicity parameter on the Si film thickness taken into account, are shown in Fig. 5. For

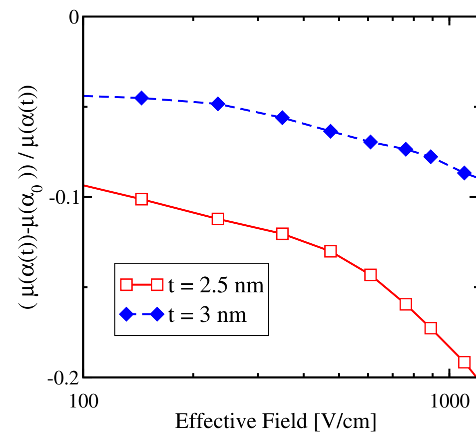

Fig. 5. Relative mobility correction due to film thickness dependence of the non-parabolicity parameter.

$t = 2.5$ nm and $t = 3$ nm the population of the primed ladder is negligible if the carrier concentration is not too large. An increase of the non-parabolicity parameter for the unprimed subbands with decreased film thickness slightly increases the scattering rates, resulting in a mobility suppression as compared to the situation with the constant bulk value α_0. The mobility correction is about 7% for $t = 3$ nm and it reaches up to 20% at high carrier concentration for $t = 2.5$ nm. The mobility decrease due to the thickness dependent non-parabolicity parameter helps to bring the simulated low field mobility in UTB FETs closer to its experimental value. Otherwise the mobility simulated with the surface roughness parameters calibrated to reproduce the universal mobility curve in inversion layers [23] is too high [24] compared to the measurement [25].

6. Conclusion

By comparing with numerical pseudopotential calculations, we demonstrated that the two-band model is valid in a larger portion of the Brillouin zone as compared to the parabolic approximation. The two-band $\mathbf{k} \cdot \mathbf{p}$ model is then used to analytically describe the subband dispersion in ultra-thin Si films, including strain. The model provides an analytical expression for the thickness-dependent non-parabolicity parameter in the unprimed subbands. Finally, the low-field mobility with the dependence of the non-parabolicity parameter on the film thickness taken into account is compared with the mobility computed with the bulk value of the non-parabolicity parameter, and relative corrections are about 7% for $t = 3$ nm and 15% for $t = 2.5$ nm.

Acknowledgement

This work has been supported by the Austrian Science Fund FWF, Projects I79-N16 and P19997-N14.

References

[1] Chau R, Doyle B, Datta S, Kavalieros J, Zhang K. Integrated nanoelectronics for the future. Nature Mater 2007;6:810–2.
[2] Rim K, Chu J, Chen H, Jenkins K, Kanarsky T, Lee K, et al. Characteristics and device design of sub-100 nm strained Si N- and PMOSFETs. In: Proceedings of theVLSI; 2002. p. 98–9.
[3] Takagi SI, Hoyt JL, Welser JJ, Gibbons JF. Comparative study of phonon-limited mobility of two-dimensional electrons in strained and unstrained Si metal–oxide–semiconductor field-effect transistors. J Appl Phys 1996;80(3):1567–77.
[4] Uchida K, Krishnamohan T, Saraswat KC, Nishi Y. Physical mechanisms of electron mobility enhancement in uniaxial stressed MOSFETs and impact of uniaxial stress engineering in ballistic regime. In: IEDM Techn. Dig.; 2005. p. 129–32.
[5] Laude LD, Pollak FH, Cardona M. Effect of uniaxial stress on the indirect excition spectrum of silicon. Phys Rev B 1971;3(8):2623–22636.
[6] Ungersboeck E, Dhar S, Karlowatz G, Sverdlov V, Kosina H, Selberherr S. The effect of general strain on band structure and electron mobility of silicon. IEEE Trans Electron Dev 2007;54(9):2183–90.
[7] Sverdlov V, Ungersboeck E, Kosina H, Selberherr S. Effect of shear strain on the conduction band in silicon: an efficient two-band $\mathbf{k} \cdot \mathbf{p}$ theory. In: Proceedings of the European solid-state device research conference; 2007. p. 386–9.
[8] Hensel JC, Hasegawa H, Nakayama M. Cyclotron resonance in uniaxially stressed silicon. II. Nature of the covalent bond. Phys Rev 1965;138(1A):A225–38.
[9] Likharev KK. Sub-20-nm electron devices. In: Morkoc H, editor. Advanced semiconductor and organic nano-techniques. New York: Academic Press; 2003. p. 239–302.
[10] Sverdlov VA, Walls TJ, Likharev KK. Nanoscale silicon MOSFETs: a theoretical study. IEEE Trans Electron Dev 2003;50(9):1926–33.
[11] Bir GL, Pikus GE. Symmetry and strain-induced effects in semiconductors. New York - York, Toronto: John Wiley & Sons; 1974.
[12] Rieger MM, Vogl P. Electronic-band parameters in strained $Si_{1-x}Ge_x$ alloys on $Si_{1-y}Ge_y$ substrates. Phys Rev B 1993;48(19):14276–87.
[13] Jacoboni C, Reggiani L. The Monte Carlo method for the solution of charge transport in semiconductors with applications to covalent materials. Rev Mod Phys 1983;55(3):645–705.
[14] VSP1.0, Vienna Schrödinger-Poisson solver 1.0 user's guide, Institut für Mikroelektronik, Technische Universität Wien, Austria 2007. <http://www.iue.tuwien.ac.at/software>.
[15] Price PJ. Resonant tunneling via an accumulation layer. Ann Phys 1981;133:217.
[16] Prange RE, Nee TW. Quantum spectroscopy of the low-field oscillations in the surface impedance. Phys Rev 1968;168(3):779–86.
[17] Fischetti MV, Ren Z, Solomon PM, Yang M, Rim K. Six-band $k \cdot p$ calculation of the hole mobility in silicon inversion layers: dependence on surface orientation, strain, and silicon thickness. J Appl Phys 2003;94(2):1079–95.
[18] Esseni D. On the modeling of surface roughness limited mobility in SOI MOSFETs and its correlation to the transistor effective field. IEEE Trans Electron Dev 2004;51(3):394–401.
[19] Jin S, Fischetti MV, Tang T-W. Modeling of surface-roughness scattering in ultrathin-body SOI MOSFETs. IEEE Trans Electron Dev 2007;54(9):2191–203.
[20] Ando T, Fowler AB, Stern F. Electronic properties of two-dimensional systems. Rev Mod Phys 1982;54(2):437–672.
[21] Smirnov S, Kosina H, Nedjalkov M, Selberherr S. Monte Carlo method for modeling of small signal response including the Pauli exclusion principle. J Appl Phys 2003;94(9):5791–9.
[22] Sverdlov V, Ungersboeck E, Kosina H, Selberherr S. Volume inversion mobility in SOI MOSFETs for different thin body orientations. Solid-State Electron 2007;51:299–305.
[23] Takagi SI, Toriumi A, Iwase M, Tango H. On the universality of inversion layer mobility in Si MOSFETs: Part I – effects of substrate impurity concentration. IEEE Trans Electron Dev 1994;41(12):2357–62.
[24] Gámiz F, Roldán JB, Godoy A, Cartujo-Cassinello P, Carceller JE. Electron mobility in double gate silicon on insulator transistors: symmetric-gate versus asymmetric-gate configuration. J Appl Phys 2003;94(9):5732–41.
[25] Uchida K, Koga J, Takagi S. Experimental study on carrier transport mechanisms in double- and single-gate ultrathin-body MOSFETs – Coulomb scattering, volume inversion, and δt_{SOI}-induced scattering. In: IEDM Techn. Dig.; 2003. p. 805–8.